Journal of Alloys and Compounds 952 (2023) 169632

Contents lists available at ScienceDirect

Journal of Alloys and Compounds

journal homepage: www.elsevier.com/locate/jalcom

Experimental and computational study on the *C*15 phase structure stability of $Y_zNi_{2-y}Mn_y$ system☆

H. Shen [a,b,c,d], S.S. Setayandeh [e,1], V. Paul-Boncour [a,2], N. Emery [a,3], Z. Li [b,c], P. Li [d], H. Yuan [b,c], L. Jiang [b,c], P.A. Burr [e,4], M. Latroche [a,5], J. Zhang [a,*,6]

[a] Univ Paris Est Creteil, CNRS, ICMPE, UMR 7182, 2 rue Henri Dunant, 94320 Thiais, France
[b] GRINM Group Co., Ltd., National Engineering Research Center of Nonferrous Metals Materials and Products for New Energy, 100088, China
[c] GRIMAT Engineering Institute Co., Ltd., 101407, China
[d] Institute for Advanced Materials and Technology, University of Science and Technology, Beijing 100083, China
[e] School of Mechanical and Manufacturing Engineering, UNSW Sydney, Sydney, NSW 2052, Australia

ARTICLE INFO

Article history:
Received 18 January 2023
Received in revised form 8 March 2023
Accepted 9 March 2023
Available online 21 March 2023

Keywords:
Laves phases
Crystal structure
Ternary diagram
DFT calculations

ABSTRACT

$Y_{0.95}Ni_2$ intermetallic is a promising candidate for hydrogen storage applications, but currently suffers from hydrogen-induced amorphization (HIA) mainly caused by its low stability. The structure stability of AB_2 Laves phase is mainly controlled by the geometric factor r_A/r_B. The present work is focused on the ternary Mn-Ni-Y system, as Mn addition helps achieving a close-to-ideal r_A/r_B (≤1.37) to avoid HIA or HID. Through a combination of X-ray diffraction, neutron diffraction, electron probe micro-analysis and first-principles calculations, new insight on the physicochemical properties and phase equilibrium of this ternary system was gained. Mn substitution is found to suppress the formation of a super-structure with ordered vacancies, in favor of a *C*15 Laves structure with a disordered distribution of Y vacancies. At low concentration Mn is accommodated only on the Ni sites, compensated by vacancies on the Y site (without long-range order). At high concentration, Mn is accommodated on both Ni and Y sites, with reduced Y vacancy concentration. The partitioning of Mn across the two sites allows to form a single-phase ternary intermetallic across a wide compositional range and suggests increased stability of the phase.

1. Introduction

The multi-structural properties of Ni-containing AB_2 Laves phase (*A* = rare earth or alkaline earth element, *B* = transition metals) give rise to lot of interest, especially for their large magnetocaloric effects [1–3] and ability to absorb hydrogen [4–6]. ANi_2 compounds crystallize in either a tetragonal La_7Ni_{16}-type (*A* = La) structure or a cubic $TmNi_2$-type (*A* = from Ce to Lu and Y) structure [7–9]. Both structures can be described as *C*15 superstructures with ordered *A* vacancies, which allow relaxing the micro strain caused by the large atomic radius ratio far to the ideal value of 1.225 (r_{La}/r_{Ni} = 1.51, r_Y/r_{Ni} = 1.45). Compounds crystallizing in $TmNi_2$-type superstructure have a lattice parameter *a* that is twice that of the parent *C*15 cubic lattice, and a lower symmetry space group $F\bar{4}3m$ [10]. Latroche et al. [4] indicated that such superstructure is widely observed in ANi_2 compounds with *A* =Pr - Lu. However, with decreasing the radius of *A* atoms, the quantity of ordered *A* vacancies on the 4*a* site diminish until reaching the 1:2 stoichiometry for $LuNi_2$. This confirms the importance of size effects in ANi_2 compounds.

Ti, Zr based AB_2 Laves type alloys are largely studied for hydrogen storage [11–14]. Rare earth based ANi_2 (*A* = rare earth) intermetallic absorb big amount of hydrogen, but currently suffers from hydrogen-induced amorphization (HIA). The mains cause of the HIA is its high atomic radius ratio r_A/r_B and the low structure stability [15,16]. It is generally known that the structural stability of AB_2 compounds can be enhanced by chemical substitution on either the *A* or *B* site. It is interesting to observe that when selected transition metals (*B* = Cu, Fe, Al) are substituted for Ni in $Y_zNi_{2-y}B_y$ (i.e. on the *B* site)[17–19], the resulting compounds favour a phase transition from

☆ With this article we honor our dear Michel Latroche who significantly contributed to this work and passed away the 30/12/2021.

* Corresponding author.
[1] 0000-0002-4875-4974
[2] 0000-0002-0601-7802
[3] 0000-0003-2724-8789
[4] 0000-0003-4796-9110
[5] 0000-0002-8677-8280
[6] 0000-0003-4978-3870

https://doi.org/10.1016/j.jallcom.2023.169632
0925-8388/

superstructure to the *C*15 Laves phase structure with a disordered arrangement of Y vacancies. Similarly, Sc substitution for Y in $Y_{0.95-x}Sc_xNi_2$ (i.e. on the *A* site) leads to the same structural transformation as $x \geq 0.5$. Furthermore, the Sc substitution for Y on the *A* site leads to a suppression of *A*-sites vacancies [20]. It is worth noting that Cu (1.28 Å), Fe (1.27 Å) and Al (1.43 Å) exhibit larger atomic radius than Ni (1.24 Å), whereas Sc (1.62 Å) exhibits smaller atomic radii than Y (1.80 Å). This suggests that modifying the average r_A/r_B ratio towards the ideal value of 1.225, leads to a stabilized *C*15 structure with or without disordered Y vacancies.

In this work, we will investigate the influence of Ni for Mn substitution in YNi_2, which is expected to lower the average r_A/r_B value due to larger Mn radius (1.35 Å). However, some previous works reported that the Mn atoms can substitute on both *A* and *B* sites in *C*15 Laves structure of the *A*-Ni-Mn compounds (*A* = Tb, Dy, Ho, Er or Zr) [21,22] and in Zr-Mn compounds with *C*14 Laves Structure [23,24], which may reduce the r_A/r_B value more drastically. For this purpose, a combination of experimental methods (EPMA, XRD, NPD, magnetics measurement) and DFT simulations is adopted to investigate the structure and phase stability of $Y_zNi_{2-y}Mn_y$ ($0.75 \leq z \leq 1$, $0.1 \leq y \leq 0.5$) compounds.

2. Experimental methods

Intermetallic compounds with nominal composition $Y_zNi_{2-y}Mn_y$ ($0 \leq y \leq 0.5$, $0.75 \leq z \leq 1$) were prepared by induction melting of high-purity metals (Y:99.9 %, Ni:99.99 %, Mn: 99.95 % from Alfa Aesar) in purified argon atmosphere (5 N) under a pressure of 0.04 MPa in a cooled copper crucible. The ingots were turned over and re-melted three times to ensure homogeneity. The as-cast ingots were subsequently annealed 3 days at 1123 K. The phase compositions and microstructure of the compounds were examined by electron probe micro-analysis (EPMA), using a CAMECA SX100.

Then, the prepared samples were mechanically crushed and ground into powder for various measurements and analysis. The samples (36 µm crushed powder) were characterized by X-ray diffraction (XRD), using a D8 DAVINCI diffractometer from Bruker with Cu-K_α radiation in the 2θ range of 10º - 100º with a step size of 0.02º. Diffraction patterns were collected at 40 kV, 40 mA for the anode of the X-ray tube. The neutron diffraction patterns were collected at room temperature on the general-purpose powder diffractometer (GPPD) at China Spallation Neutron Source (CSNS). The XRD and NPD patterns were analyzed via joint Rietveld method by using the package TOPAS [25].

3. Computational methods

$Y_zNi_{2-y}Mn_y$ structures were generated by substituting 1–5 Mn on the Ni and Y sites, and 1–3 vacancies on the Y site, of a perfect $2 \times 1 \times 1$ supercell of YNi_2 with *C*15 Laves structure. To account for configurational entropy, which is expected to play a dominant role in a system that undergoes order/disorder transitions, all possible permutations of Mn and vacancy defects configurations were considered within our supercell, and the configurational entropy was obtained using ensemble averaging techniques [26]. The site-occupancy disorder (SOD) program [27] was used to obtain all symmetrically-unique permutations of defects (Mn_{Ni}, Mn_Y and $\square_Y$). The resulting 3374 structures were relaxed using density functional theory (DFT) as implemented in the Vienna Ab Initio simulation program (VASP) [28–30]. All DFT simulations used the PBE exchange-correlation functional [31,32], with a plane-wave cut-off of 350 eV and **k**-point grid of $2 \times 4 \times 4$ [33]. A first-order Methfessel-Paxton smearing function [34] of width 0.1 eV was applied to treat partial occupancies of bands. All simulations were energy minimized at constant pressure, with convergence criteria of 10^{-6} eV and 10^{-5} eV for electronic and ionic minimization, respectively.

The effective enthalpy and effective lattice parameter of an ensemble containing N configurations are:

$$E_f = \sum_{n=1}^{N} P_n E_n \tag{1}$$

$$a = \sum_{n=1}^{N} P_n a \tag{2}$$

where P_n is the ensemble probability of occupying a particular configuration with degeneracy of Ω_n and formation enthalpy of E_n, calculated as [1].

$$P_n = \frac{\Omega_n \exp(-\frac{E_n}{k_B T})}{\sum_{n=1}^{N} \Omega_n \exp(-\frac{E_n}{k_B T})} \tag{3}$$

Enthalpy of formation from standard state was calculated as

$$E_n = \frac{\mu(\text{Comp.}) - (x)\mu(\text{Y}) - (y)\mu(\text{Ni}) - (z)\mu(\text{Mn})}{x + y + z} \tag{4}$$

where μ is the chemical potentials of the compound and reference phases, taken as the DFT total energy of a unit cell of the reference metals in their elemental ground state (hcp-Y, bcc-Ni and α-Mn.

The Gibbs free energy of formation at any given temperature *T* was calculated as:

$$G_f = E_f - TS^{conf.} \tag{5}$$

where $S^{conf.}$ is configurational entropy calculated as:

$$S^{conf.} = k_B \sum_{n=1}^{N} P_n \ln P_n \tag{6}$$

4. Experimental and computational results

4.1. Synthesis and phase occurrence

As shown in Fig. 1, we initially prepared two series of compounds: $Y_{0.9}Ni_{2-y}Mn_y$ ($0.1 \leq y \leq 0.5$) and $Y_zNi_{1.7}Mn_{0.3}$ ($0.75 \leq z \leq 1.00$), then $Y_{0.95}Ni_2$, $Y_{0.86}Ni_{1.8}Mn_{0.2}$ and $Y_{0.79}Ni_{1.61}Mn_{0.39}$.

The Rietveld analyses of the XRD patterns of $Y_zNi_{1.7}Mn_{0.3}$ ($0.75 \leq z \leq 1.00$) and $Y_{0.9}Ni_{2-y}Mn_y$ ($0.1 \leq y \leq 0.5$) were performed with the assumption that Mn atom could occupy only the Ni-site and that

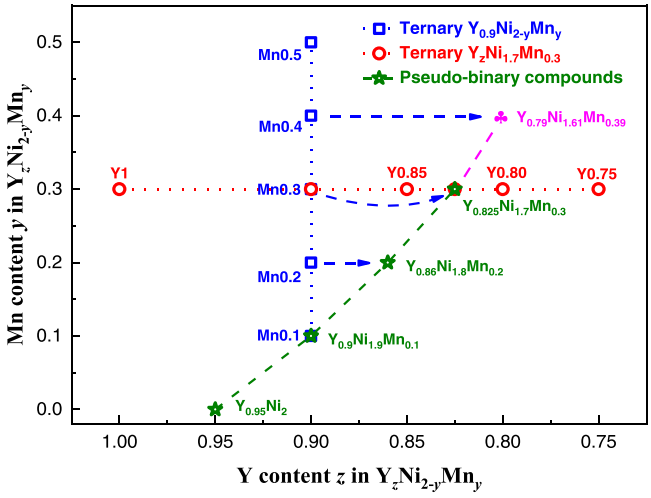

Fig. 1. The experimental compositions of $Y_zNi_{2-y}Mn_y$ compounds: the blue squares represent $Y_zNi_{1.7}Mn_{0.3}$ compounds; the red circles represent $Y_{0.9}Ni_{2-y}Mn_y$ compounds; the green stars represent the $Y_zNi_{2-y}Mn_y$ compounds with single-phase *C*15-type structure ($Y_{0.95}Ni_2$: superstructure); the magenta symbol represents $Y_{0.79}Ni_{1.61}Mn_{0.39}$ compound with *C*15 as main phase.

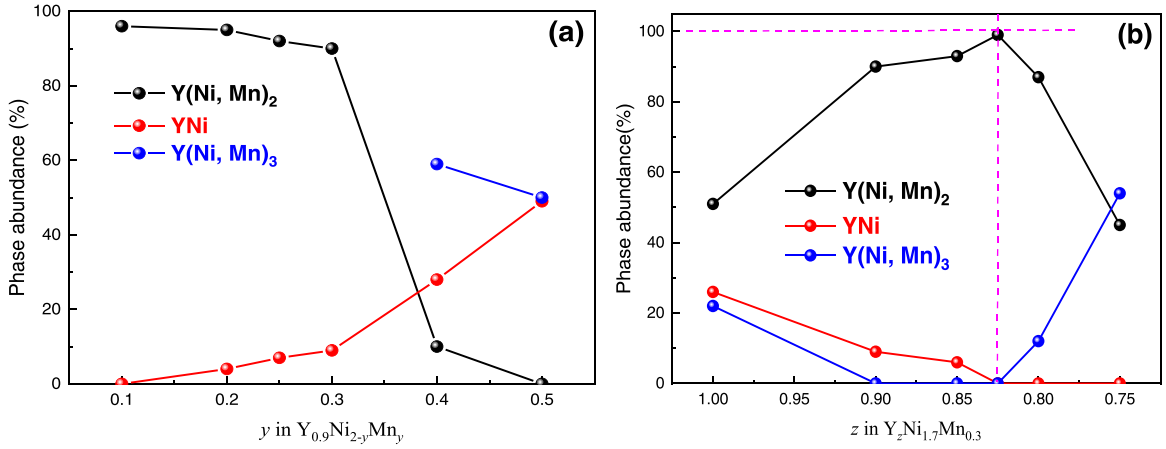

Fig. 2. Phase abundance of Y(Ni, Mn)$_2$, YNi and Y(Ni, Mn)$_3$ as function of Mn content (a) and Y content (b), in $Y_{0.9}Ni_{2-y}Mn_y$ and $Y_zNi_{1.7}Mn_{0.3}$ compounds respectively.

the Y-site could be partially vacant, the figures are given in the supplementary information (Fig. S.1 – Fig. S.4) and the obtained results are given in Table S.1- Table S.2.

From XRD patterns, no superstructure was observed for all Mn-containing samples. Fig. 2 shows the phase abundance from Rietveld refinement as the function of the Y content $0.75 \le z \le 1.00$ ($y = 0.3$) and nominal Mn content for $0.1 \le y \le 0.5$ ($z = 0.9$).

For $Y_{0.9}Ni_{2-y}Mn_y$ ($0.1 \le y \le 0.3$) alloys, *C*15 Laves phase Y(Ni, Mn)$_2$ appears as the main phase. Abundance of the Y(Ni, Mn)$_2$ phase decreases slowly with the increasing Mn content and vanishes for $y = 0.5$. Conversely, YNi (*AB*-type, space group *Pnma*, No. 62) appears as the secondary phase and its abundance increases monotonously with the increasing Mn content from $y = 0.1$ to $y = 0.5$. Meanwhile, Y(Ni, Mn)$_3$ (*AB*$_3$-type, space group $R\bar{3}m$, No. 166) replaces *C*15 phase as the main phase for $y = 0.4$ and 0.5. Consequently, the solubility limit of Mn in *AB*$_2$ phase in $Y_{0.9}Ni_{2-y}Mn_y$ is around $y = 0.4$.

For $Y_zNi_{1.7}Mn_{0.3}$ ($0.75 < z \le 1.00$) alloys, *C*15 Laves phase Y(Ni, Mn)$_2$ is always the main phase. The secondary phases *AB*-type YNi and *AB*$_3$-type Y(Ni, Mn)$_3$ form depending on Y content. The amount of YNi phase is positively associated with Y content. Abundance of the YNi phase falls with *z* deceasing from 1 to 0.825 and disappears for $z = 0.825$. A reverse trend is observed for *AB*$_3$-type phase, as when *z* decreases from 0.825 to 0.75, Y(Ni, Mn)$_3$ phase appears. According to Rietveld analysis, its amount increases from 0 to 54 wt %. It is worth noting that we can also observe 22 wt % of the Y(Ni, Mn)$_3$ phase for $z = 1$. Formation of the Y(Ni, Mn)$_3$ phase here can be interpreted as the chemical balance due to the formation of 26 wt % of YNi phase. For $z = 0.825$, single *C*15 phase is obtained for the given Mn content $y = 0.3$.

The XRD patterns of $Y_{0.95}Ni_2$, $Y_{0.9}Ni_{1.9}Mn_{0.1}$, $Y_{0.86}Ni_{1.8}Mn_{0.2}$; $Y_{0.825}Ni_{1.7}Mn_{0.3}$, $Y_{0.79}Ni_{1.6}Mn_{0.4}$ alloys are presented in Fig. 3. The four first compounds are single phase and the last one contains a small amount of *AB*$_3$ phase. $Y_{0.95}Ni_2$ presents a single $TmNi_2$-type phase with the previously described superstructure (space group $F\bar{4}3m$, No. 216) [5,35]. The Mn-substituted compounds with nominal compositions $Y_{0.9}Ni_{1.9}Mn_{0.1}$, $Y_{0.86}Ni_{1.8}Mn_{0.2}$ and $Y_{0.825}Ni_{1.7}Mn_{0.3}$ all crystallize in the *C*15 Laves phase structure without any superstructure peaks (Fig. 4). Then a mixture of *C*15 and *AB*$_3$-type Y(Ni, Mn)$_3$ phase was observed for $Y_{0.79}Ni_{1.61}Mn_{0.39}$, which further indicates the solubility of Mn in *AB*$_2$ phase should be around $y = 0.4$.

Assuming that the Mn atoms substitute only Ni atoms, and the vacancies are on the Y-site, the XRD patterns are refined with Rietveld method. The relevant crystallographic data, composition and the calculated density and chemical compositions measured by EPMA are summarized in Table 1. Rietveld refinement reveals that the lattice parameter increases with Mn content. With the assumption that Mn and vacancies occupy different sublattices (Ni and

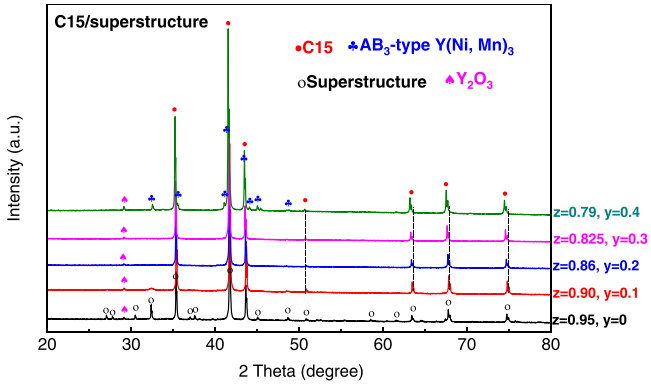

Fig. 3. XRD patterns of $Y_{0.95}Ni_2$, $Y_{0.9}Ni_{1.9}Mn_{0.1}$, $Y_{0.86}Ni_{1.8}Mn_{0.2}$, $Y_{0.825}Ni_{1.7}Mn_{0.3}$, $Y_{0.79}Ni_{1.6}Mn_{0.4}$ compounds.

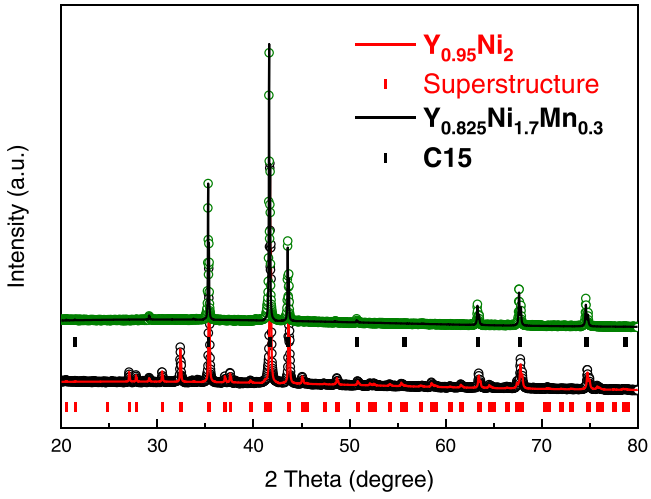

Fig. 4. The superstructure and *C*15 structure respectively formed in $Y_{0.95}Ni_2$ and $Y_{0.825}Ni_{1.7}Mn_{0.3}$ compounds.

Y, respectively), the refined vacancy content is not regular: it first increases, then decreases and increase again with Mn content, which does not coincide with the nominal Y content. This may indicate that the above assumptions are not exact and that Mn and/or vacancies can occupy both sublattices to some degree. This cannot be achieved reliably on the XRD patterns due to limited scattering contrast between Mn, Ni and Y. Thus, an unconstrained Rietveld refinement was performed on the NPD patterns presented below.

Table 1
Crystallographic data and chemical compositions for $Y_zNi_{2-y}Mn_y$ compounds with single *C*15 phase structure.

Y	Composition EPMA (± 0.01)	Crystal structure	*a* (Å)	*V* (Å^3)	*Y-site occupation %*	Composition (diffraction)
0	$Y_{0.95}Ni_{2.00}$	Superstructure	14.3557 (3) /7.1778 (1)	2958.55 (9) /369.81 (1)	96(1)	$Y_{0.96}Ni_2$
0.1	$Y_{0.86}Ni_{1.87}Mn_{0.13}$	*C*15	7.1733 (1)	369.11 (1)	85(1)	$Y_{0.85}Ni_{1.87}Mn_{0.13}$
0.2	$Y_{0.85}Ni_{1.79}Mn_{0.21}$	*C*15	7.1826 (1)	370.55 (1)	83(1)	$Y_{0.83}Ni_{1.79}Mn_{0.21}$
0.3	$Y_{0.825}Ni_{1.68}Mn_{0.32}$	*C*15	7.1912 (1)	371.88 (1)	87(1)	$Y_{0.87}Ni_{1.68}Mn_{0.32}$
0.4	$Y_{0.80}Ni_{1.59}Mn_{0.41}$	*C*15	7.2001(1)	373.27(1)	84(1)	$Y_{0.84}Ni_{1.59}Mn_{0.41}$

4.2. Structural properties of the C15 Laves phase

4.2.1. Cell parameter

Fig. 5 shows cell parameter variation versus Mn content, obtained via DFT simulation (Fig. 5a) and experiment (Fig. 5b). In panel (a), each data point corresponds to the ensemble average of cell parameters of all configurations at that composition, calculated via Eq. 2, at 500 K. Noting that each average value is the results of hundreds of DFT simulations, where the cell parameters of lowest energy configurations have relatively larger weight in the ensemble average. An increasing trend is observed in the cell dimension with increasing the content of Mn from 0.1 to 0.3. The smaller lattice constant obtained for $(Y_{0.94}\square_{0.06})(Ni_{1.88}Mn_{0.12})$ (will be discussed later) relative to YNi_2 is partly owed to the existence of more vacancies in this structure. Further increase of Mn content increases the lattice parameter slowly, with a rate that deviates strongly from the Vegard's low applied to the end members YNi_2 and YMn_2. Experimentally, the same tendance is observed: the lattice parameter of $Y_{0.9}Ni_{1.9}Mn_{0.1}$ is smaller than the binary compound $Y_{0.95}Ni_2$ and then it increases with further Mn additions. For comparison, the lattice parameter of YMn_2 and the Ni substituted compound $YMn_{1.8}Ni_{0.2}$ with *C*15 structure reported in the literature [36] are also plotted. Clearly, the slope of the lattice parameter change with Mn content is very low for $Y_{0.9}Ni_{2-y}Mn_y$ in comparison with that of $YMn_{2-x}Ni_x$.

Fig. 6 shows ternary diagram of cell parameter as function of composition obtained by EPMA, indicating the domain of *C*15 phase formation. It increases with Mn content before decreasing again and reaches the limit of solubility of Mn around 0.15 corresponding to the composition $Y_{0.8}Ni_{1.6}Mn_{0.4}$. A strong correlation is observed between lattice parameter and composition along "*b*" direction, where the lattice parameters increase with the Mn content while the Y content is constant. The changes of lattice parameter can be interpreted as a solid solution behavior. Following the "a_1" direction, within low Mn content range, the lattice parameter remains unchanged if Y content decreases tinnily accompanied with the Mn content increasing. Similarly, for the compositions with high Mn content, along "a_2" direction, the Ni content is basically unchanged, while the Y content decreases significantly the lattice parameter remains unchanged. This three-dimension behavior indicates a more "complex" structure than we assumed before.

4.2.2. Site occupation

The contrast between Mn and Ni atoms is not sufficient by XRD, whereas neutron diffraction allows to discriminate between Ni and Mn and localize Mn on Ni site. Therefore, time of flight neutron diffraction was performed at 300 K for $Y_{0.9}Ni_{1.9}Mn_{0.1}$, $Y_{0.86}Ni_{1.8}Mn_{0.2}$, $Y_{0.825}Ni_{1.7}Mn_{0.3}$ and $Y_{0.79}Ni_{1.61}Mn_{0.39}$ single phase samples.

To better distinguish the occupations of vacancies and Mn, the neutron powder diffraction and laboratory XRD patterns are jointly analyzed and are based on the following hypotheses: the yttrium, nickel and manganese content are fixed to the value determined by EPMA, the Y atoms occupy only *A*-site, the Ni atoms occupy only *B*-sites, while the refinement allows to distribute Mn atoms within *A* and *B* sites, keeping the sum $(m{\cdot}Mn(A) + (1-m){\cdot}Mn(B))$ equal to EPMA measured content, by fitting only the parameter *m*. The total occupancy of the *A*-site is also refined, to account for possible vacancies (□). The *A*/*B* ratio is fixed to the stoichiometry 1/2 as Eq. (7).

$$(Y + \square + m{\cdot}Mn)/(Ni + (1-m){\cdot}Mn) = \frac{1}{2} \quad (7)$$

Fig. 7 presents the Rietveld refinement of the neutron powder diffraction (a), and the XRD (b) of $Y_{0.825}Ni_{1.7}Mn_{0.3}$. The joint Rietveld analysis of NPD and XRD of all other compounds are shown in Fig. S.6 in the supplementary information. The detailed information of atomic occupations and lattice parameters from refined XRD and NPD patterns are listed in Table 2. For the low Mn content sample $y = 0.1$, the Y-site is occupied with Y (86 %) and vacancies (14 %), while Mn occupies only Ni-site. For all other Mn contents, the Mn atoms occupy both *A*-site and *B*-sites and no more vacancies are present in the structure.

4.2.3. DFT calculation

Fig. 8 represents the composition of the compounds investigated computationally (empty symbols), and experimentally (filled symbols) the dashed line is for guide eyes to illustrate the experimentally studied domain. In total, thirty-six compositions of (Y, Mn)(Ni, $Mn)_2$ were simulated in the range of 20–35 at %Y, 55–74 at %Ni and 0–11 at %Mn.

Fig. 9 represents predicted Gibbs free energy of formation of compounds (Y, □, Mn)(Ni, $Mn)_2$ in the composition range of 10.42–10.87 at %Mn (a), 8.33–8.88 at %Mn (b) and 6.25–6.52 at %Mn (c), calculated with Eq. 1, at 500 K to weigh each compound by its corresponding configurational degeneracy. Stability of each compound was then assessed on the basis of a convex hull, which is a line that connects the lowest energy compounds in any composition range of interest. Any compound that does not lie on the convex hull is deemed metastable. The effect of ensemble temperature on the trend of stability was found to be negligible (see Fig. S.7 in supplementary material).

In the composition range of 6.25–6.52 at %Mn, the compound $(Y_{0.88}\square_{0.12})(Ni_{1.81}Mn_{0.19})$ has the lowest formation enthalpy. This compound contains 12.5 % Y vacancy, with all Mn atoms occupy Ni sites. At higher Mn content of 8.33–8.88 at %, the lowest enthalpy compound is $(Y_{0.81}Mn_{0.13}\square_{0.06})(Ni_{1.88}Mn_{0.12})$, which contains 6.25 % Y vacancy and 50 % of Mn atoms occupy Y sites. At even higher Mn content of 10.42–10.87 at %, $(Y_{0.81}Mn_{0.13}\square_{0.06})(Ni_{1.81}Mn_{0.19})$ possesses

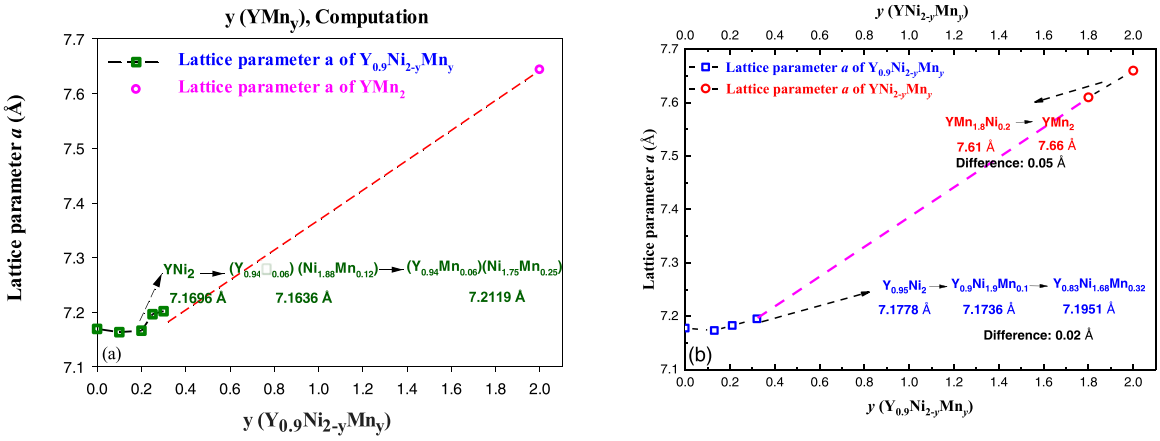

Fig. 5. Cell parameter variation versus Mn content, obtained via DFT simulation (a) and experiment (b).

the lowest formation enthalpy. This compound contains 6.25 % Y-site vacancy with roughly around 40 % of Mn atoms occupy the Y sites. Notably, compounds with no vacancies, or with too many vacancies on the Y sites are unfavourable in these composition ranges.

The distribution of Mn and Y vacancies for the three most stable compositions is shown in Fig. 10. Our simulations reveal that Mn may be accommodated on both Y and Ni sites, however, the partitioning between the two sites is strongly dependent on Mn content: at low content (< 6.52 at %Mn), Mn is preferentially accommodated on the Ni sites only. At higher Mn content (8.33–10.87 at %Mn), Mn atoms may be accommodated on both sites. Additionally, it is found that vacancies on Y sites are indispensable for stabilizing (Y,□)(Ni,Mn)$_2$, which is dominant at low Mn content.

The magnetic measurements of the single phase samples were performed using a conventional Physical Properties Measurement System (PPMS) from Quantum Design. $Y_{0.95}Ni_2$ is paramagnetic in agreement with previous work [37]. We have observed that the Mn for Ni substitution did not induce a significant change of the magnetic properties. This behavior proves that the magnetic consideration is not necessary for DFT calculation.

5. Discussion

The $Y_zNi_{2-y}Mn_y$ have been studied by combined powder diffraction techniques (X-ray and neutron), EPMA and DFT simulations. The data analyses show that upon Mn substitution, the $Y_zNi_{2-y}Mn_y$ compounds crystalize with a disordered *C*15 structure rather than the ordered superstructure of $Y_{0.95}Ni_2$. For $z = 0.9$, the Mn content y varies from 0.1 to 0.5. It was found that single-phase compound can only be obtained with $y = 0.1$. For each given Mn content, alloys with different z values were synthesized. It was found that with increasing of Mn content y, the stoichiometry z should be decreased to obtain single phase. For $y = 0.2$, 0.3 and 0.4, the *C*15 phase forms with large sub-stoichiometric $z = 0.86$, 0.825 and 0.79 respectively.

To explain this phenomena, we propose two hypothesis: i) the Y-site vacancy, which is supported by the presence of *A*-site vacancies in ANi_2 compounds (*A*= rare earth elements) already reported by [6–8,17,35,38], ii) the Mn occupation of *A* site, which is supported by the ability of Mn to sit on the *A* sites in $ZrMn_2$-type Laves phase, allowing large over-stoichiometric domains $ZrMn_{2+x}$ [22,23]. Moreover, ternary RNi_2Mn (*R* = Tb, Dy, Ho, Er) compounds [21,39] crystalize in the *C*15 Laves phase structure, where Mn occupies both *A*-sites and *B*-sites.

The phases composition obtained by EPMA for all studied compounds are shown in the ternary diagram (Fig. 11). The homogeneity

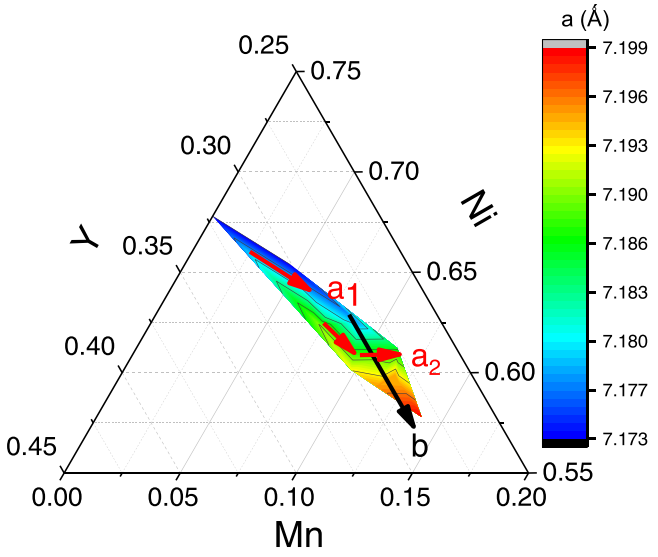

Fig. 6. Lattice parameter a of the *C*15 Laves phase in the ternary diagram of Y-Ni-Mn.

region of the (Y,Mn)(Ni,Mn)$_2$ phase is surrounded by dashed line and those of AB_3 phases are framed by two blue lines. The points of YNi phase are shown in black squares. AB_2 phases coexist with *AB* and AB_3 neighbouring phases for the multi-phase samples. This is a tentative phase diagram. It is shown that the AB_2 phase domain varies with Mn content. At low Mn content, the phase forms with narrow stoichiometry. With increasing of Mn content, the composition region becomes wider up to the limit around $y \approx 0.4$. It is worth noting that all AB_2 compositions measured here contain less Y than the ideal Y(Ni, Mn)$_2$ stoichiometry. This implies the presence of vacancies on the Y-site, or the presence of Mn substitution on Y-site, or both. The compositions of ternary AB_3 phases locate around the stoichiometry Y(Ni, Mn)$_3$ line without large deviations. *AB* (YNi) phase is very low in Mn and it can be considered as a binary compound with negligible Mn solubility (Fig. 11).

Experimentally, the laboratory XRD provides a good resolution of the structure to determine the lattice parameters but could not distinguish Ni and Mn occupations due to their very similar electron cloud. The neutron diffraction, specially by TOF technique gives a higher resolution of the atomic occupation. By using TOPAS package, a joint refinement of XRD and NPD allowed us to determine the Mn occupation and eventually *A*-site vacancies. The diffraction refinement revealed a similar trend to those predicted by DFT simulations.

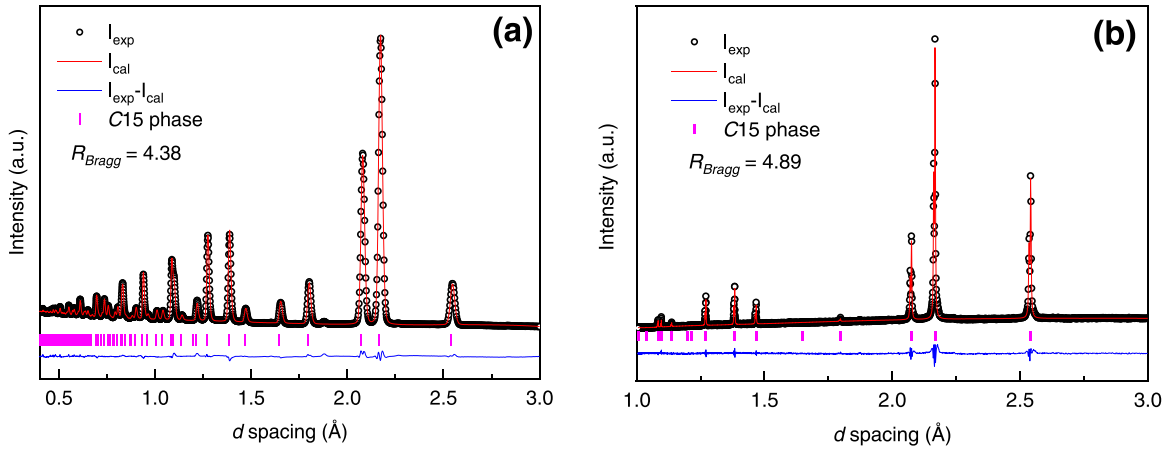

Fig. 7. The Rietveld analyses of the NPD (a) and XRD (b)of $Y_{0.825}Ni_{1.7}Mn_{0.3}$ compound by joint refinement.

Table 2
Detailed structural information of *C*15 phases with the nominal composition $Y_{0.9}Ni_{1.9}Mn_{0.1}$, $Y_{0.86}Ni_{1.8}Mn_{0.2}$ and $Y_{0.825}Ni_{1.7}Mn_{0.3}$ and $Y_{0.79}Ni_{1.61}Mn_{0.39}$ from joint NPD and XRD refinement.

Nominal Composition		$Y_{0.9}Ni_{1.9}Mn_{0.1}$	$Y_{0.86}Ni_{1.8}Mn_{0.2}$	$Y_{0.825}Ni_{1.7}Mn_{0.3}$	$Y_{0.79}Ni_{1.61}Mn_{0.39}$
Wykoff site 8b	Y	86(1)	90(1)	88(2)	86(1)
(3/8, 3/8, 3/8)	Mn	0	10(1)	12(1)	14(1)
atom occ.%	□	14(1)			
Wykoff site 16c	Ni	94(1)	95(1)	89(1)	85(2)
(0, 0, 0)	Mn	6(1)	5(1)	11(1)	15(1)
atom occ.%					
Composition from diffraction		$Y_{0.86}□_{0.14}Ni_{1.87}Mn_{0.13}$	$Y_{0.9}Mn_{0.1}Ni_{1.89}Mn_{0.11}$	$Y_{0.88}Mn_{0.12}Ni_{1.78}Mn_{0.22}$	$Y_{0.86}Mn_{0.14}Ni_{1.7}Mn_{0.3}$
Composition EPMA		$Y_{0.86}Ni_{1.87}Mn_{0.13}$	$Y_{0.85}Ni_{1.79}Mn_{0.21}$	$Y_{0.825}Ni_{1.68}Mn_{0.32}$	$Y_{0.80}Ni_{1.59}Mn_{0.41}$
a (Å)		7.1736 (1)	7.1813 (1)	7.1861 (1)	7.1998 (1)

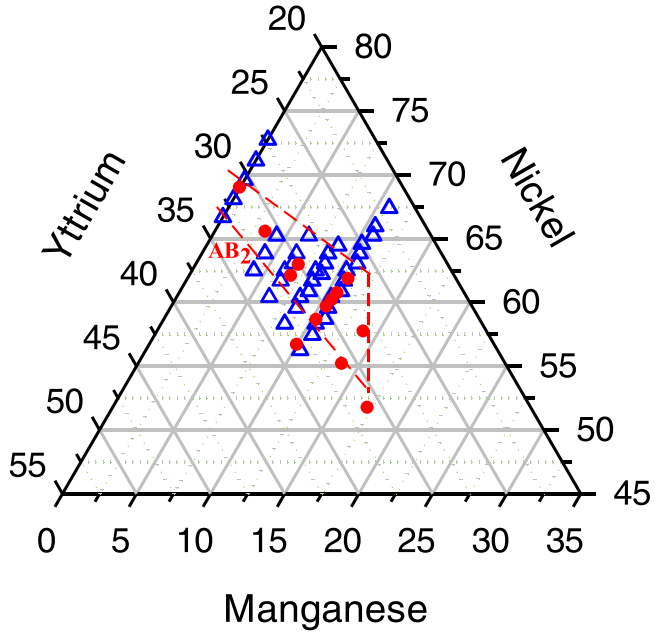

Fig. 8. Ternary plot of the simulated compositions of (Y, □, Mn)(Ni, Mn)$_2$ (empty symbols), together with the compositions of the samples synthesized experimentally (filled symbols), the dashed line is for guide eyes to illustrate the experimentally studied domain.

Noting, however, that a direct comparison of the exact same compositions was impossible due to the practical limitation of the number of atoms that can be modelled in DFT. At low Mn content, the Mn occupation of Y can be neglected as the structure is stabilized by the Y-site vacancies, 14 % of the Y-sites are vacant. This high-concentration of vacancy can explain the smaller lattice parameter of $Y_{0.9}Ni_{1.9}Mn_{0.1}$ compared to the binary compound $Y_{0.95}Ni_2$, which contains only 5 % Y vacancies [5]. Despite of the larger atomic radius of Mn compared to Ni, the larger proportion of vacancies in $Y_{0.9}Ni_{1.9}Mn_{0.1}$ (14 %) leads to a slight lattice contraction. At high Mn content, the vacancies on the *A*-sites decrease drastically and eventually disappear, instead 64 %, 56 % and 48 % of Mn atoms occupy the *A*-sites in $Y_{0.85}Ni_{1.79}Mn_{0.21}$, $Y_{0.825}Ni_{1.68}Mn_{0.32}$ and $Y_{0.80}Ni_{1.59}Mn_{0.41}$, respectively (see Table 2). This results to an almost constant Mn-on-Y substitution rate (10 %, 13 % and 14 % respectively) while a significant increase of the Mn content on the *B*-site (5.5 %, 10 % and 15 % respectively) globally leads to a lattice parameter increase. The results from DFT simulations are in good agreement with experimental results: at low Mn content the *C*15 is stabilized by *A*-site vacancies. DFT calculation shows that at high Mn content, the vacancies percentage decreases and Mn atoms occupy both *A* and *B*-sites (*A*-sites occupation of 50 % and 40 % for $Y_{0.81}Ni_{1.88}Mn_{0.28}$ and $Y_{0.81}Ni_{1.81}Mn_{0.32}$, respectively). At high Mn content, *C*15 phase can be formed in a wider composition domain, compensated by the partitioning of Mn substitution sites, as clearly indicated in Fig. 11. Also, the constant lattice parameter of *C*15 phase in the direction "*a*2″ shown in Fig. 6 indicates the material's ability to adjust Mn partitioning between sites. This behavior is confirmed by the DFT calculation results: for a given concentration of Mn, several compositions

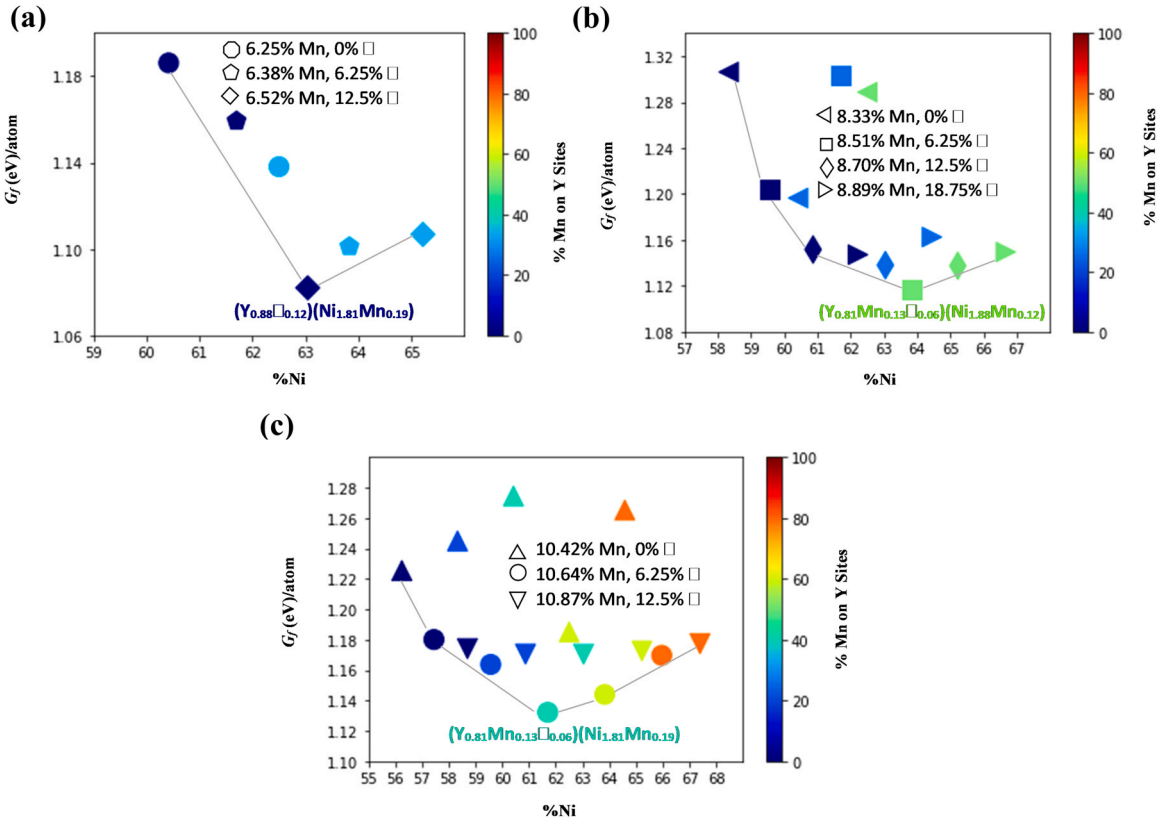

Fig. 9. Gibbs free energy of formation of compounds of (Y,□,Mn)(Ni,Mn)$_2$ at 500 K, in the composition range of (a) 6.25–6.52 at %Mn; (b) 8.33–8.88 at %Mn and (c) 10.42–10.87 at % Mn, color-coded by %Mn accommodated on the Y sites.

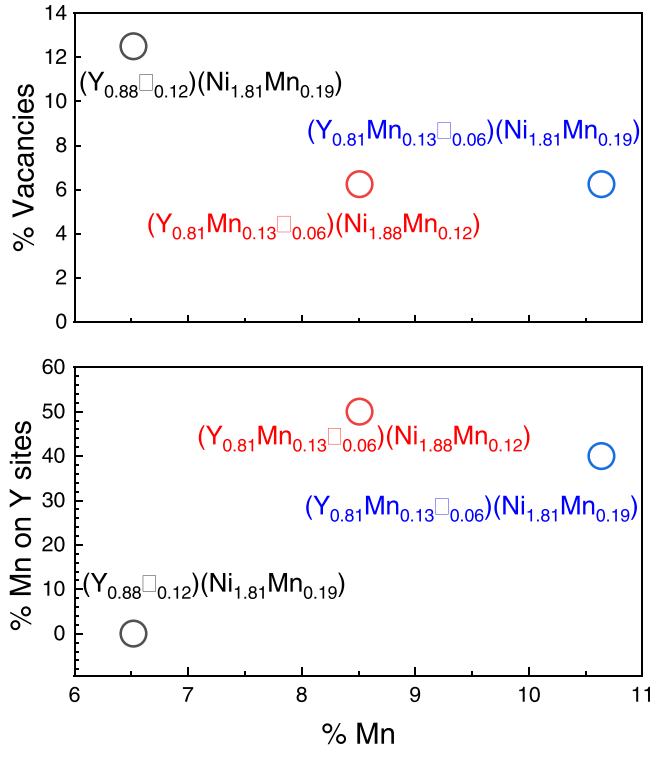

Fig. 10. Percentage of vacancy on Y sites (upper panel) and Mn atoms occupy Y sites (lower panel).

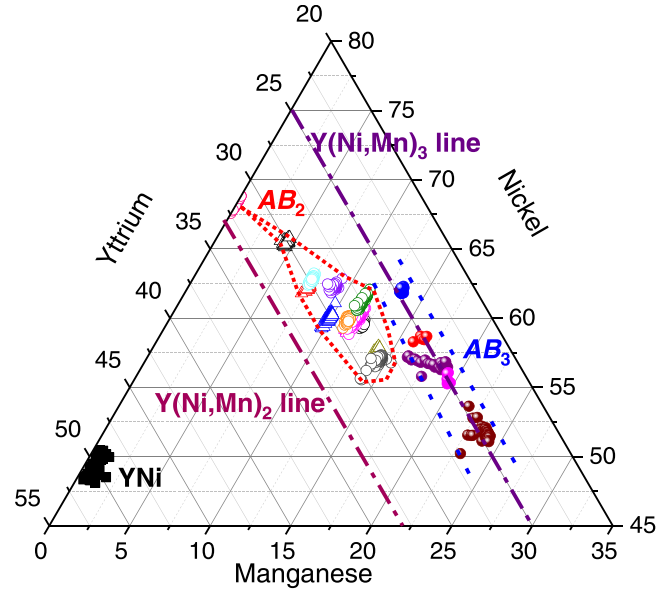

Fig. 11. Ternary diagram of $Y_zNi_{2-y}Mn_y$ compounds: the opened symbols represent AB_2 phase; the closed balls represent AB_3 phase; the closed black boxes represent YNi phase, the homogeneity region of the (Y,Mn)(Ni,Mn)$_2$ phase is surrounded by the red dashed line.

with varying degree of Ni and vacancies have similar Gibs free energy (Fig. 9), and these structures form with different partitioning of Mn on Ni and Y sites.

6. Conclusions

By combining different characterization techniques (standard X-ray diffraction, neutron diffraction, EPMA) and DFT simulations, the phase formation and site occupation for Ni substitution by Mn atoms in the systems $Y_zNi_{2-y}Mn_y$ was clarified. $Y_zNi_{2-y}Mn_y$ compound crystalizes in *C*15 with disordered Y-site vacancies at low Mn content. When Mn content increases to around 10 at %, the *C*15 phase forms with Mn occupying both Y and Ni sites. Furthermore, this phase can be formed over a wide composition range, enabled by a self-adjusting partitioning of Mn on the Y and Ni sites, compensated by Y vacancies. This phase, in which the average atomic radius ratio r_A/r_B is close to 1.37, might be a promising candidate for reversible hydrogen storage. Further works on their hydrogenation properties will be undertaken.

CRediT authorship contribution statement

H. Shen: Data curation; Formal analysis; Investigation; Writing - original draft, Writing - review & editing, S. S. Setayandeh: Computation, Methodology, Formal analysis, Writing - original draft, Writing - review & editing, V. Paul-Boncour: Writing - original draft, Writing - review & editing., N. Emery: data curation, review & editing, Z. Li: Funding acquisition, Supervision., L. Jiang: Funding acquisition, Supervision, P. Li: Editing, H. Yuan: Editing, P. A. Burr: Methodology, Formal analysis, Writing – review & editing, Funding acquisition, Supervision, M. Latroche: Funding acquisition; Methodology, Junxian Zhang: Conceptualization, Formal analysis, Writing - original draft, Writing - review & editing, Funding acquisition, Supervision.

Data availability

Data will be made available on request.

Declaration of Competing Interest

The authors declare that they have no known competing financial interests or personal relationships that could have appeared to influence the work reported in this paper.

Acknowledgment

This work is supported by the Campus France under Cai Yuanpei project 44027 WH. We are thankful to E. Leroy for the EPMA analysis, China Spallation Neutron Source for the neutron diffraction and financial support from French-Australian network IRN-FACES. SSS and PAB would like to acknowledge Tokamak Energy (UK) for providing financial support. This work was undertaken with the assistance of resources and services from the National Computational Infrastructure (NCI), which is supported by the Australian Government; the Pawsey Supercomputing Centre, which is supported by the Australian Government and the Government of Western Australia; and was enabled by Intersect Australia Limited (www.intersect.org.au).

Appendix A. Supporting information

Supplementary data associated with this article can be found in the online version at doi:10.1016/j.jallcom.2023.169632.

References

[1] D.P. Shoemaker, C.B. Shoemaker, Concerning the relative numbers of atomic coordination types in tetrahedrally close packed metal structures, Acta Cryst. B. 42 (1986) 3–11, https://doi.org/10.1107/S0108768186098671

[2] E. Gratz, A. Kottar, A. Lindbaum, M. Mantler, M. Latroche, V. Paul-Boncour, M. Acet, C. Barner, W.B. Holzapfel, V. Pacheco, K. Yvon, Temperature- and pressure-induced structural transitions in rare-earth-deficient (*R* = Y, Sm, Gd, Tb) Laves phases, J. Phys.: Condens. Matter 8 (1996) 8351–8361, https://doi.org/10.1088/0953-8984/8/43/026

[3] E. Gratz, E. Goremychkin, M. Latroche, G. Hilscher, M. Rotter, H. Müller, A. Lindbaum, H. Michor, V. Paul-Boncour, T. Fernandez-Diaz, New magnetic phenomena in $TbNi_2$, J. Phys.: Condens. Matter 11 (1999) 7893–7905, https://doi.org/10.1088/0953-8984/11/40/314

[4] M. Latroche, V. Paul-Boncour, A. Percheron-Guégan, Structural instability in $R_{1-x}Ni_2$ compounds and their hydrides (*R* = Y, Rare Earth), Z. Für Phys. Chem. 179 (1993) 261–268, https://doi.org/10.1524/zpch.1993.179.Part_1_2.261

[5] A. Percheron-Guégan, V. Paul-Boncour, M. Latroche, J.C. Achard, F. Bourée-Vigneron, Structure of $Y_{0.95}Ni_2$ and its hydride, J. Less Common Met. 172–174 (1991) 198–205, https://doi.org/10.1016/0022-5088(91)90448-D

[6] V. Paul-Boncour, A. Percheron-Guegan, M. Diaf, J.C. Achard, Structural characterization of RNi_2 (R = La, Ce) intermetallic compounds and their hydrides, J. Less Common Met. 131 (1987) 201–208, https://doi.org/10.1016/0022-5088(87)90518-2

[7] V. Paul-Boncour, A. Lindbaum, M. Latroche, S. Heathman, Homogeneity range and order–disorder transitions in $R_{1-x}Ni_2$ Laves phase compounds, Intermetallics 14 (2006) 483–490, https://doi.org/10.1016/j.intermet.2005.08.003

[8] V. Paul-Boncour, A. Lindbaum, Ab initio calculations on the formation of $La_{1-x}Ni_2$, Compd., J. Phys.: Condens. Matter 14 (2002) 3921, https://doi.org/10.1088/0953-8984/14/15/306

[9] A. Lindbaum, J. Hafner, E. Gratz, Ab initiostudies of the formation of a $Y_{1-x}Ni_2$superstructure with ordered Y vacancies, J. Phys.: Condens. Matter 11 (1999) 1177–1187, https://doi.org/10.1088/0953-8984/11/5/006

[10] A.F. Deutz, R.B. Helmholdt, A.C. Moleman, D.B. De Mooij, K.H.J. Buschow, Superstructure in the intermetallic compound $TmNi_2$, J. Less Common Met. 153 (1989) 259–266, https://doi.org/10.1016/0022-5088(89)90120-3

[11] V.A. Yartys, M.V. Lototskyy, Laves type intermetallic compounds as hydrogen storage materials: a review, J. Alloy. Compd. 916 (2022) 165219, https://doi.org/10.1016/j.jallcom.2022.165219

[12] T. Maeda, T. Fuura, I. Matsumoto, Y. Kawakami, M. Masuda, Cyclic stability test of AB_2 type (Ti, Zr)(Ni, Mn, V, Fe)$_{2.18}$ for stationary hydrogen storage in water contaminated hydrogen, J. Alloy. Compd. 580 (2013) S255–S258, https://doi.org/10.1016/j.jallcom.2013.03.230

[13] U. Ulmer, M. Dieterich, A. Pohl, R. Dittmeyer, M. Linder, M. Fichtner, Study of the structural, thermodynamic and cyclic effects of vanadium and titanium substitution in laves-phase AB_2 hydrogen storage alloys, Int. J. Hydrog. Energy 42 (2017) 20103–20110, https://doi.org/10.1016/j.ijhydene.2017.06.137

[14] M. Kandavel, V.V. Bhat, A. Rougier, L. Aymard, G.-A. Nazri, J.-M. Tarascon, Improvement of hydrogen storage properties of the AB_2 Laves phase alloys for automotive application, Int. J. Hydrog. Energy 33 (2008) 3754–3761, https://doi.org/10.1016/j.ijhydene.2008.04.042

[15] K. Aoki, X.-G. Li, T. Masumoto, Factors controlling hydrogen-induced amorphization of *C*15 Laves compounds, Acta Metall. Mater. 40 (1992) 1717–1726, https://doi.org/10.1016/0956-7151(92)90115-U

[16] U.-I. Chung, Y.-G. Kim, J.-Y. Lee, General features of hydrogen-induced amorphization in RM_2 (*R* = rare earth, *M* = transition element) Laves phases, Philos. Mag. B (2006), https://doi.org/10.1080/13642819108207589

[17] V. Paul-Boncour, A. Lindbaum, E. Gratz, E. Leroy, A. Percheron-Guégan, Structural study of the pseudobinary $Y(Ni, Cu)_2$ system, Intermetallics 10 (2002) 1011–1017, https://doi.org/10.1016/S0966-9795(02)00120-6

[18] O. Myakush, V. Babizhetskyy, P. Myronenko, H. Michor, E. Bauer, B. Kotur, Influence of doping elements (Cu and Fe) on the crystal structure and electrical resistivity of YNi_3 and $Y_{0.95}Ni_2$, Chem. Met. Alloy. 4 (2011) 152–159, https://doi.org/10.30970/cma4.0181

[19] H. Shen, V. Paul-Boncour, M. Latroche, F. Cuevas, P. Li, H. Yuan, Z. Li, J. Zhang, L. Jiang, Investigation of the phase occurrence and H sorption properties in the $Y_{33.33}Ni_{66.67-x}Al_x$ ($0 \le x \le 33.33$) system, J. Alloy. Compd. 888 (2021) 161375, https://doi.org/10.1016/j.jallcom.2021.161375

[20] S. Zhao, H. Wang, J. Liu, Exploring the hydrogen-induced amorphization and hydrogen storage reversibility of $Y(Sc)_{0.95}Ni_2$ laves phase compounds, Materials 14 (2021) 276, https://doi.org/10.3390/ma14020276

[21] J.L. Wang, C. Marquina, M.R. Ibarra, G.H. Wu, Structure and magnetic properties of RNi_2Mn compounds (*R* = Tb, Dy, Ho, and Er), Phys. Rev. B 73 (2006) 094436, https://doi.org/10.1103/PhysRevB.73.094436

[22] B. Houvert, Diagramme d'equilibre zirconium-manganese-Nickel à 1173 K, Fixation d'hydrogène sur especes métalliques de ce systeme, Université des sciences et techniques du Languedoc, 1984.

[23] R.M. van Essen, K.H.J. Buschow, Composition and hydrogen absorption of *C*14 type Zr-Mn compounds, Mater. Res. Bull. 15 (1980) 1149–1155, https://doi.org/10.1016/0025-5408(80)90079-3

[24] J.-L. Bobet, B. Darriet, Relationship between hydrogen sorption properties and crystallography for $TiMn_2$ based alloys, Int. J. Hydrogen Energy 25 (2000) 767–772, https://doi.org/10.1016/S0360-3199(99)00101-9

[25] TOPAS, General Profile and Structure Analysis Software for Powder Diffraction Data, version 4.2; Bruker, AXS GmbH, Karlsruhe, Germany, TOPAS, General Profile and Structure Analysis Software for Powder Diffraction Data, version 4.2, (n.d.).

[26] S.L. Dudarev, G.A. Botton, S.Y. Savrasov, C.J. Humphreys, A.P. Sutton, Electron-energy-loss spectra and the structural stability of nickel oxide: An LSDA+U study, Phys. Rev. B. 57 (1998) 1505–1509, https://doi.org/10.1103/PhysRevB.57.1505

[27] R. Grau-Crespo, S. Hamad, C.R.A. Catlow, N.H. de Leeuw, Symmetry-adapted configurational modelling of fractional site occupancy in solids, J. Phys.: Condens. Matter 19 (2007) 256201, https://doi.org/10.1088/0953-8984/19/25/256201
[28] G. Kresse, J. Hafner, Ab initio molecular dynamics for liquid metals, Phys. Rev. B 47 (1993) 558–561, https://doi.org/10.1103/PhysRevB.47.558
[29] G. Kresse, J. Hafner, Ab initio molecular-dynamics simulation of the liquid-metal–amorphous-semiconductor transition in germanium, Phys. Rev. B. 49 (1994) 14251–14269, https://doi.org/10.1103/PhysRevB.49.14251
[30] G. Kresse, J. Furthmüller, Efficiency of ab-initio total energy calculations for metals and semiconductors using a plane-wave basis set, Comput. Mater. Sci. 6 (1996) 15–50, https://doi.org/10.1016/0927-0256(96)00008-0
[31] P.E. Blöchl, Projector augmented-wave method, Phys. Rev. B. 50 (1994) 17953–17979, https://doi.org/10.1103/PhysRevB.50.17953
[32] J.P. Perdew, K. Burke, M. Ernzerhof, Generalized gradient approximation made simple, Phys. Rev. Lett. 77 (1996) 3865–3868, https://doi.org/10.1103/PhysRevLett.77.3865
[33] H.J. Monkhorst, J.D. Pack, Special points for Brillouin-zone integrations, Phys. Rev. B. 13 (1976) 5188–5192, https://doi.org/10.1103/PhysRevB.13.5188
[34] M. Methfessel, A.T. Paxton, High-precision sampling for Brillouin-zone integration in metals, Phys. Rev. B. 40 (1989) 3616–3621, https://doi.org/10.1103/PhysRevB.40.3616
[35] M. Latroche, V. Paul-Boncour, A. Percheron-Guégan, J.C. Achard, Structure determination of $Y_{0.95}Ni_2$ by X-ray powder diffraction, J. Less Common Met. 161 (1990) L27–L31, https://doi.org/10.1016/0022-5088(90)90334-G
[36] K. Fujiwara, Effect of hydrogen absorption on the magnetic properties of pseudobinary intermetallics $Y(Mn_{1-x}T_x)_2$ (T=Al, Co and Ni), J. Phys. Soc. Jpn. 57 (1988) 2133–2142, https://doi.org/10.1143/JPSJ.57.2133
[37] J. Ćwik, T. Palewski, K. Nenkov, N.V. Tristan, J. Warchulska, G.S. Burkhanov, O.D. Chistyakov, Some physical properties of $Y_xHo_{1-x}Ni_2$ solid solutions, J. Alloy. Compd. 373 (2004) 78–85, https://doi.org/10.1016/j.jallcom.2003.11.016
[38] M. Latroche, V. Paul-Boncour, A. Percheron-Guegan, J.C. Achard, Deviations from the C15 type structure in RNi_2 compounds (R = Y, Ce), Eur. J. Solid State Inorg. Chem. 28 (1991) 597–600.
[39] J.L. Wang, C.C. Tang, G.H. Wu, Q.L. Liu, N. Tang, W.Q. Wang, W.H. Wang, F.M. Yang, J.K. Liang, F.R. de Boer, K.H.J. Buschow, Structure and magneto-history behavior of $DyNi_2Mn$, Solid State Commun. 121 (2002) 615–618, https://doi.org/10.1016/S0038-1098(02)00041-8